Journal of the Royal Society Interface
Electronic Supplementary Material

Flight efficiency is a key to diverse wing morphologies in small insects

Thomas Engels[1], Dmitry Kolomenskiy[2], Fritz-Olaf Lehmann[1,*]

[1]Department of Animal Physiology, Institute of Biosciences, University of Rostock, Germany, Albert-Einstein-Str. 3, 18059 Rostock

[2]Center for Design, Manufacturing and Materials, Skolkovo Institute of Science and Technology, Moscow, 121205, Russia

* Author for correspondence

8 figures (Figs S1-S8), 1 table (Table S1), 10 pages

Section 1: Reconstruction of bristle distribution at model wing

Figure S1 shows details on the construction of model wings. If not mentioned otherwise, all wing dimensions are normalized to wing length R. The planform is a 'snowcone' shape with a circle radius R_t=0.23 at the wing tip and two tangents intersecting the membrane at distance L_r=0.054 from the root. The solid membrane is rectangular with length L_m=0.77 and width B_m=0.068. Bristles were attached according to two rules: (i) bristles at the wing tip that continuously rotated around the tip and (ii) parallel oriented bristles along the sides of the membranous section (Fig. S1). The origin of tip bristles is at the centre of a virtual circle (Fig. S1, magenta lines), placed at an offset L_{off}=0.075 from the end of the membrane. The virtual circle has a radius $R_t + L_{off}$. Consecutive bristles are rotated by increment $\Delta\alpha$ and arc length of the virtual circle equal to $2\Delta b$. Bristle spacing was doubled at the tip of the membranous section because we found that bristles interfere at the tip when using a step width Δb. The angle between parallel bristles and membrane was α_b = 29° and bristle diameter and membrane thickness were 7.7×10^{-3}. The solid wing had a surface of 0.289 R^2. The various geometrical parameters of the model are chosen to visually resemble the wings in Fig. 1, and in particular the *G. ficorum* (thrips) wing. We aim at providing a well-defined geometrical model for reproducibility and do not expect variations in its parameters to have a significant impact on the conclusions of our work.

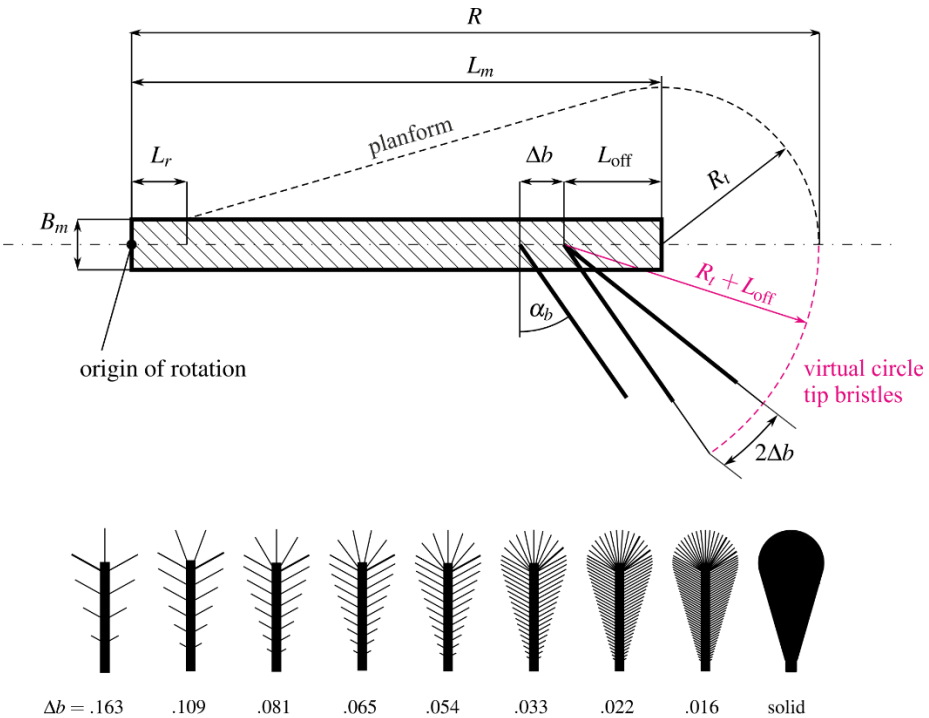

Figure S1. Top: Parameters for the construction of model wings with various bristle spacing Δb. See text for details. Bottom: the various wing models used in the study.

The dimensions of the model wing were adopted from the 4-winged species shown in figure 1*a*. *Kikiki huna* and *Tinkerbella nana* are the smallest flying insects known so far, with 245 and 354 µm wing length, respectively (Table S1) [1]. These species have bristled wings with a small membranous section. Wingbeat frequency and kinematics are unknown. The wasp *E. formosa* was extensively studied by Weis-Fogh [2]. The wasp *E. mundus* is parasitic to the sweet potato whitefly *Bemisia tabaci* (Hemiptera) that is a phytophagous pest of many agricultural crops. *E. mundus* and *E. formosa* have hybrid wings that consist of a large membrane with short bristles. The laurel thrips *Gynaikothrips ficorum* (Thysanoptera) is the largest species included in this study. Its wings have numerous long bristles and a small solid membrane area. We only considered the forewings of the species in our study because the hindwings of wasps are typically smaller than forewings. *B. tabaci* has 4 similar-sized membranous wings.

Table S1. Wing morphology, kinematics, and Reynolds number considered in this study (cf Fig. 1). Bristle length is measured at wing tip and characteristic angle of lateral bristles with respect to the wing's longitudinal axis at the shaft's mid length (red, Fig. 1). p.c., personal communication with Gal Ribak, Tel Aviv University; n.a., not applicable or unknown; Ref, reference; Re, Reynolds number based on *Rf*.

Species	Ref	Wing type	Wing length (µm)	Bristle number	Bristle angle (degrees)	Bristle spacing Δb	Bristle length L_B	Wingbeat frequency (Hz)	*Re*
Kikiki huna	[1]	bristled	245	30	61.6	0.06*R*	0.310*R*	n.a.	n.a.
Megaphragma caribea	[3]	bristled	286	32	77.9	0.054*R*	0.280*R*	n.a.	n.a.
Tinkerbella nana	[1]	bristled	354	40	50.6	0.048*R*	0.289*R*	n.a.	n.a.
Eretmocerus mundus	[4], p.c.	hybrid	600	78	46.6	0.016*R*	0.057*R*	273	7
Encarsia formosa	[2, 5]	hybrid	642	82	64.8	0.02*R*	0.055*R*	361	10
Bemisia tabaci	p.c.	solid	1012	0	n.a.	n.a.	n.a.	131	7
Gynaikothrips ficorum	p.c.	bristled	1460	173	54.9	0.0125*R*	0.101*R*	196	24
Model wing		bristled	n.a.	9 - 99	61	see text	0.224*R*	see text	4 - 57

Section 2: Bristle elasticity and bending

In our simulation we modelled a solid wing because calculations suggested negligible bending during flapping flight. The following approach describes how we derived an upper estimate of bristle bending at maximum wing flapping velocity. The bristle is modelled as a clamped beam sticking out at the wing tip (Fig. 1). The bristle is attached to a membranous section and faces a uniform load. The bending line tangent at the attachment point has thus zero slope. The bristle (beam) with length L and diameter d_B is immersed in air with density ρ=1.225 Kgm^{-3} and kinematic viscosity ν=1.225 m^{2}s^{-1}. We used L=198 µm, is the maximum bristle length measured in a bristled wing, and d_B was 1.82 µm (*Paratuposa placentis* [6]; *cf.* figure 1). Second moment of bristle inertia, I, was derived from the equation:

$$I = \frac{\pi}{4}\left(\frac{d_B}{2}\right)^4. \qquad \text{(eq. S1)}$$

In root-flapping wings, maximum instantaneous velocity is largest at the wing tip. Thus, for simplicity, we modelled bristle bending in response to a uniform, constant, maximum free stream velocity u_∞. If u_∞ equals wing tip velocity $u_{tip}=Rf$, flow velocity is 0.16 ms^{-1} (*E. mundus*), 0.23 ms^{-1} (*E. formosa*), and 0.28 ms^{-1} (*G. ficorum*). At a maximum stroke amplitude of 180°, these velocities convert to 1.0, 1.45, and 1.76 ms^{-1}, respectively, using $u_{tip}=2\Phi Rf$ (see section 5, Table S1). For comparison, own measurements in *Paratuposa placentis* (body length 395 µm) suggest a maximum wing tip velocity of ~1.4 ms^{-1} and ~0.45ms^{-1} at the radius of gyration. Elasticity was considered using Young's modulus E=5.5 GPa for the cuticle of insect wings [7].

We further assumed that the mass of the bristle is negligible and thus its inertial force in front of the forces exerted by the fluid. Bristle bending was estimated from drag based on a coefficient for a cylinder's 2D circular cross section [6, 8], i.e.:

$$C_D = \frac{4\pi\delta}{Re_B} \cdot \frac{4}{1+\sqrt{1+4.3\delta^2}}, \qquad \text{(eq. S2)}$$

with Re_B the Reynolds number for the bristle and δ defined as:

$$\delta = \frac{1}{0.5 - 0.577216 - \ln(0.125\,Re_B)} \text{ and } Re_B = \frac{u_\infty d_B}{\upsilon}. \qquad \text{(eq. S3)}$$

Force per unit bristle length, F', is eventually derived from conventional aerodynamic theory, written as:

$$F' = \frac{1}{2}\rho C_D u_\infty^2 d_B. \qquad \text{(eq. S4)}$$

Due to viscous coupling between bristles, bending a single bristle differs from bending a group of bristles. As viscous coupling increases with decreasing Reynolds number, this coupling needs to be considered. Cheer and Koehl [9], however, suggested that the force on a bristle in a group is always smaller than on an isolated bristle. We thus modelled only a single bristle and eqs. 2-5 thus provide an upper estimate for maximum bristle bending.

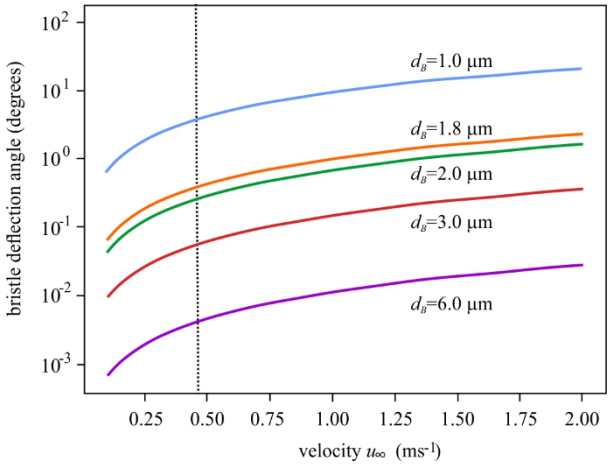

Figure S2. Bristle tip deflection angle as a function of the free stream velocity and bristle diameter. Vertical dashed line is mean velocity at the radius of gyration in *Paratuposa placentis*.

For static bending, maximum wing tip deflection of a bristle y_{max} is:

$$y_{max} = \frac{F' L^4}{8EI}. \qquad \text{(eq. S5)}$$

Figure S2 shows beam tip deflection as a function of bristle diameter and velocity. In *Paratuposa placentis* (orange, Fig. S2), maximum bristle deflection is 10 µm or ~5-times the bristle diameter. The latter value converts into less than ~3° root-tip deflection of a single bristle. Thicker bristles bend increasingly less because their stiffness scales with $\sim d_B^4$, while aerodynamic load only with $\sim d_B$. Even very small bristles with d_B=1 µm and facing 0.45 ms^{-1} flow velocity deflect only little (~3.8°). At ~1.4 ms^{-1} wing tip velocity of *Paratuposa placentis*, a 1 µm thin bristle deflects ~15°. We conclude that bristles should not significantly deflect during flapping flight and may be thus considered as stiff for CFD modelling and robotic experiments.

Section 3: Wing kinematics

Lift-based kinematics were modelled by functions previously proposed for wing flapping by Toomey [10]. This family of functions uses the angles ϕ and α in which parameter σ_ϕ controls the shape of ϕ (sinusoidal to sawtooth) and σ_α the shape of α (sinusoidal to heaviside). We used values of $\sigma_\phi = 5$ and $\sigma_\alpha = 4$. The functions (Fig. 2*a*, top) are given as:

$$\phi = \frac{150°}{2} \frac{G_t + 0.5}{\max(|G_t + 0.5|)} \qquad \text{(eq. S6)}$$

$$\alpha = -45° \cdot G_r(t) \qquad \text{(eq. S7)}$$

with the auxiliary functions [10]:

$$G_t(t) = \frac{\int_0^t \tanh\left(\sigma_\phi \cos(2\pi\tau+\frac{\pi}{2})\right)d\tau}{\max\left(\left|\int_0^t \tanh\left(\sigma_\phi \cos(2\pi\tau+\frac{\pi}{2})\right)d\tau\right|\right)} \quad \text{(eq.S8)}$$

$$G_r(t) = \frac{\tanh\left(\sigma_\alpha \cos(2\pi\tau+\frac{\pi}{2})\right)}{\max\left(\left|\tanh\left(\sigma_\alpha \cos(2\pi\tau+\frac{\pi}{2})\right)\right|\right)}. \quad \text{(eq. S9)}$$

The wing moved in a horizontal stroke plane with zero deviation angle, and stroke amplitude was 150° with symmetrical wing rotation (±0.2 cycle duration) at the stroke reversals. Mean wing tip velocity u_{tip} was 5.2Rf with f the wingbeat frequency.

Drag-based kinematics were modelled according to the kinematics of the tiny beetle *Nephanes titan* [11]. Wing tip path is a figure-of-eight motion that is divided into two phases per half stroke. The wing's angle of attack is approximately zero during stroke reversals and 90° during the up- and downstroke. We modelled this kinematics by functions proposed by Suzuki [12]. In their notation, the functions (Fig. 1a middle) are given as

$$\phi' = \phi_m \cos(2\pi t) \quad \text{(eq. S10)}$$

$$\alpha' = 0.5 \cdot \alpha_m(1 + \cos(2\pi t + \gamma)) \quad \text{(eq. S11)}$$

with $\phi_m = 90°$, $\gamma = 90°$ and $\alpha_m = 90°$. Using a nonlinear optimization toolbox available in python, this convention has been converted to the three Euler angles as defined in [13]. The resulting functions cannot be given in analytical form and are shown in Fig. 1a (bottom). The mean wing tip velocity u_{tip} is 7.5 Rf.

Section 4: Clap-and-fling kinematics

For clap-and-fling kinematics we used lift-based kinematics with 180° flapping amplitude. Thus, clap-and-fling conditions occurred twice in each stroke cycle. At the stroke reversals, the wings were parallel with 0.04R distance between the left and right wing surface. Angle of attack during translation was 45° with wing rotational phases at the reversals lasting ±0.2 stroke cycle. Feathering angle (orange, Fig. S3) at the transitions was slightly smoothed compared to the single wing kinematics to avoid wing-wing collisions.

Section 5: Reynolds number

To allow comparisons with previous studies in insect flight, Reynolds number Re was determined from reference velocity U and calculated as:

$$Re = \frac{UR}{\nu}, \quad \text{(eq. S12)}$$

with ν the kinematic viscosity of air. In our study, we computed flows at Reynolds numbers 4, 14, and 57 that covers the Reynolds numbers estimated for insects in figure 1a-g up to the size of a fruit fly. In contrast to previous studies, reference velocity in eq. S12 was derived as U=Rf and is thus independent from stroke amplitude. We chose this velocity scale because the stroke amplitude is unknown in these animals. Length scale in eq. S12 is wing length R instead of mean wing chord [14] because c_m is difficult to reliably define in the bristles wings shown in Fig. 1. Conventional Reynolds number Re= ν^{-1} u_{tip} c_{m} with u_{tip}=2$\Phi f R$ (Φ, stroke amplitude) and mean wing chord c_{m} is 1.7 and 2.4-times higher for the lift- and drag-based kinematics, respectively, than the values above. Reynolds number for bristles was calculated as:

$$Re_{bristle} = \frac{d_B R f}{\nu}, \quad \text{(eq. S13)}$$

with d_{B} the diameter of a bristle and f the flapping frequency.

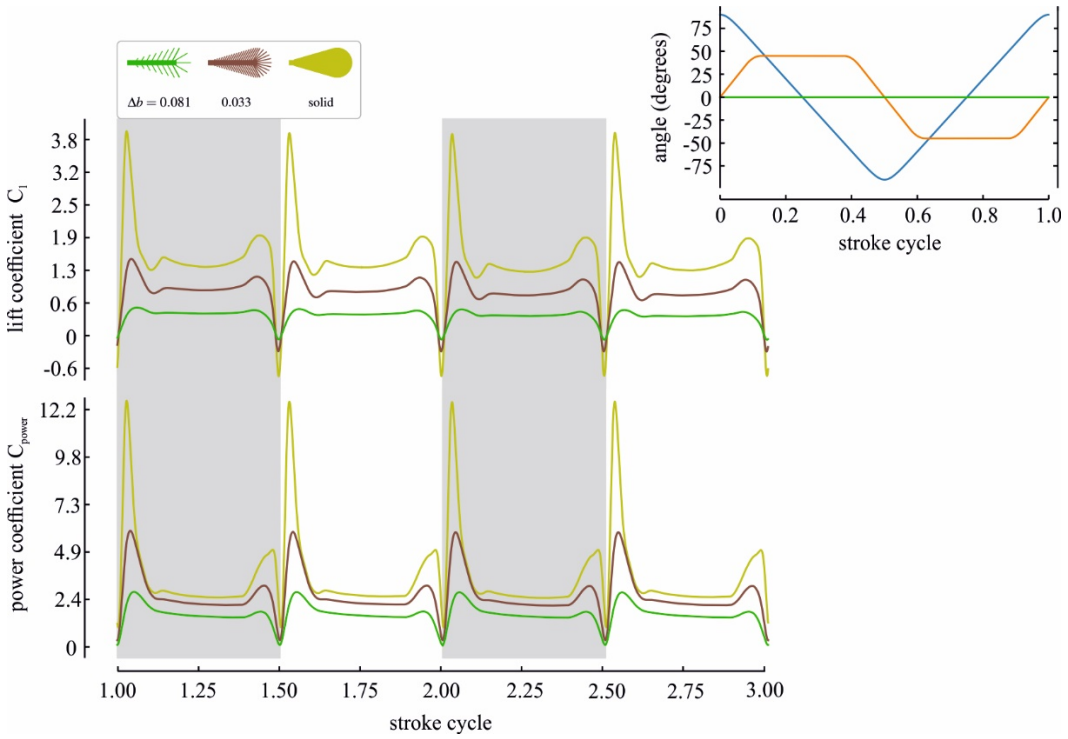

Figure S3. Lift- and power coefficients during two stroke cycles of two wings while flapping left and right one with clap-fling-sweep kinematics. Inset on the right shows clap-and-fling kinematics with horizontal flapping angle (blue), rotational (orange; feathering, angle of attack) angle, and vertical heaving motion (green). Reynolds number is *Re*=14.

Section 6: Numerical simulation

6.1 Numerical method

The WABBIT code uses explicit second order finite differences to solve the artificial compressibility equations [15]:

$$\partial_t \underline{u} + \underline{u}\cdot\nabla\underline{u} + \nabla p - \nu\nabla^2\underline{u} + \frac{\chi}{C_\eta}(\underline{u}-\underline{u}_s) + \frac{\chi_{sp}}{C_{sp}}(\underline{u}-\underline{u}_\infty) = 0 \qquad \text{(eq. S14)}$$

$$\partial_t p + C_0^2\nabla\cdot\underline{u} + \frac{\chi_{sp}}{C_{sp}}(p-p_\infty) = 0. \qquad \text{(eq. S15)}$$

This approximation of the incompressible Navier-Stokes equations [16] introduces a constant artificial speed of sound C_0 much larger than fluid velocity. Its explicit nature avoids solving large linear systems in every time step. Boundary conditions are imposed using the volume penalization method that has extensively been used to study insect flight [17]. It treats a solid wing as a porous medium with vanishing permeability C_η. An indicator function χ is used to distinguish between the fluid (where χ = 0) and wing domain (where χ = 1). Near the boundary, a smoothing layer is required in case of moving objects such as a wing. Permeability is coupled to grid resolution Δx by:

$$C_\eta = \frac{(K_\eta \Delta x)^2}{\nu}, \qquad \text{(eq. S16)}$$

with K_η a constant that depends weakly on Reynolds number. In the present computation K_η was 0.5 because of low Reynolds number. We used a similar technique to model non-reflecting outflow boundary conditions at the outer border of the cubical computational domain of size L. This so-called sponge term χ_{sp}/C_{sp} imposes far field conditions and absorbs outgoing pressure waves.

Despite the inhibition of turbulence at low Reynolds numbers, numerical simulations of bristled wings are challenging because of the vast range of scales. Flow structures like the leading edge vortex, for example, are several orders of magnitude larger than the scale of an individual bristle that hinders three-dimensional simulations [18]. To overcome this limitation, we here developed a numerical framework using wavelet-based grid refinement. Starting from an uniform coarse grid, we doubled the number of grid points J_{max} times until reaching the desired

precision. Grid refinement was done in a block-based fashion. The computational grid thus consists of blocks of size B_s^3, with spatial resolution:

$$\Delta x = \frac{2^{-J_{max}} \cdot L}{B_s - 1}, \qquad \text{(eq. S17)}$$

in the zones of maximum refinement (Fig. S4). Second order lifted Cohen-Daubechies-Feauveau wavelets (CDF 2/2) are used for grid refinement in locations at which the magnitude of the wavelet coefficients was larger than a threshold C_ϵ. Refinement was executed as follows: we first performed a coarse simulation using a low value of $J_{\max}$ with numerical parameters C_0 and C_ϵ based on previous numerical simulations [19]. Refinement was then improved by increasing C_0 and decreasing C_ϵ, C_η according to convergence properties. This procedure ensured convergence of the solution toward a wing composed of solid, impermeable material immersed in an incompressible, viscous fluid.

The coupling of permeability and resolution yields small values for permeability that imposed small and thus an elevated number of time steps Δt in previous studies [20]. We circumvented this problem in bristled wing simulations by employing custom Runge-Kutta-Chebychev (RKC) schemes for explicit time integration [21-22]. These schemes allowed us to set Δt dependent on C_0, and in particular as $\Delta t > C_\eta$. Moreover, we only simulated wings and excluded the animal body. The origin of wing rotation was at the centre of the numerical domain, all simulations started from a quiescent fluid and were simultaneously computed by up to 480 CPU cores of a supercomputer.

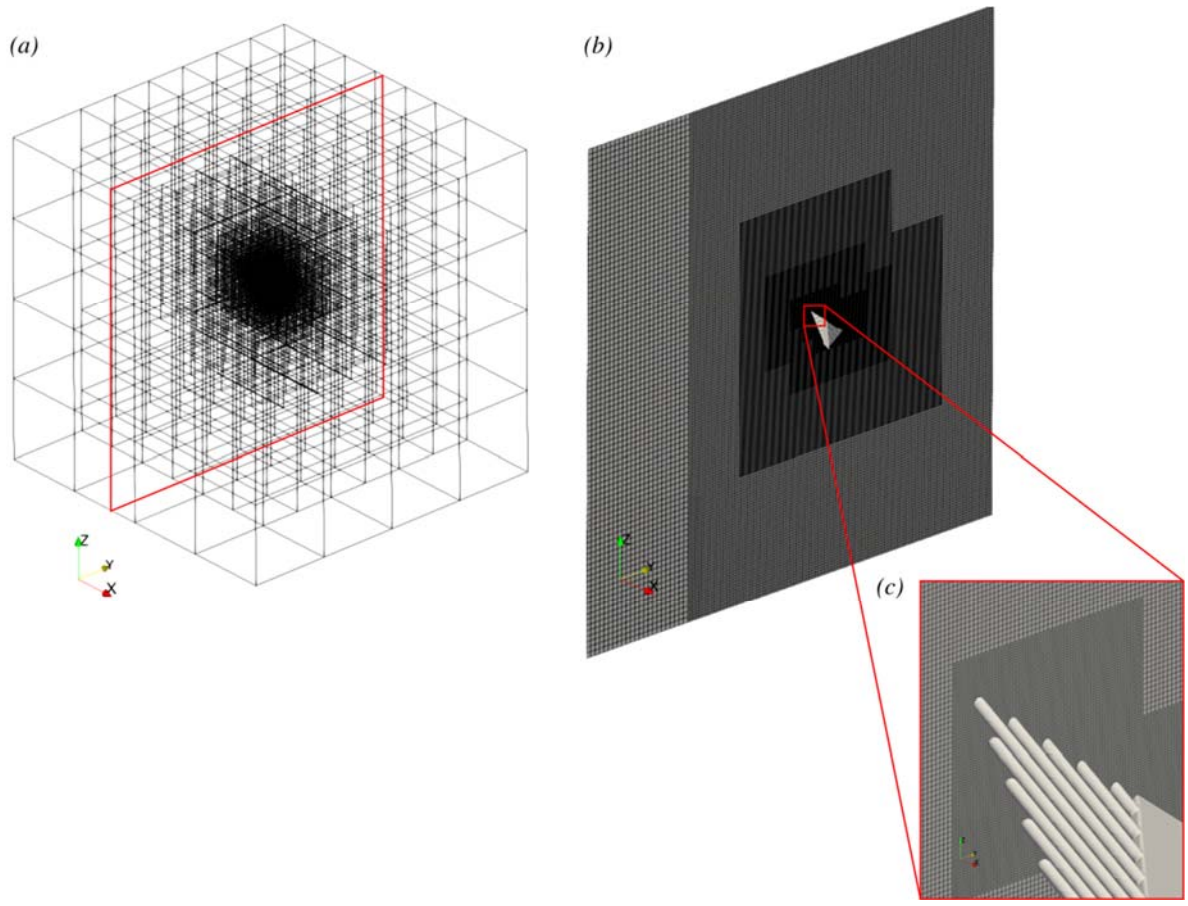

Figure S4. Numerical method for the simulation of bristled wings. (*a*) Spatial domain for computing, showing complete 3D grid with grid lines representing blocks and not points. Each block comprises 23 grid points. The grid shows the increasing local grid refinement towards the domain centre that holds the modelled wing. (*b*) Two-dimensional cut, showing the wing and individual grid points. (*c*) Zoom on the grid points near the bristles

6.2 Temporal discretization with Runge-Kutta-Chebychev methods

Like fourth-order Runge-Kutta schemes, RKC methods are explicit multistep methods. RKC family schemes are characterized by number of stages s and damping parameter $\in$. Regardless of s, a fixed number of 7 registers is required for the right hand side, making this method more memory-efficient than Krylov subspace methods. For each simulation, we used the following custom RKC scheme: we programmed a one-dimensional discrete operator for the artificial compressibility equation (ACM) in Python. This operator had the same second order discretization as used in the complete 3-dimensional simulation. The underlying grid was Cartesian and equidistant. As $C_0 >> |\underline{u}|$, we neglected the nonlinear term in ACM. The discrete operator included the Laplacian, pressure gradient, penalization, and the transport term of the pressure equation. The complex eigenvalues λ of this operator matrix were used to determine the best RKC scheme. Specified time step was:

$$\Delta t = CFL \cdot \frac{\Delta x}{C_0}, \qquad \text{(eq. S18)}$$

with CFL=0.75. For all scaled eigenvalues $2\lambda\Delta t$ with a safety factor of two, we computed growth rate P_j to determine stable RKC schemes [22]. We eventually selected the RKC scheme with least stages (smallest s) and largest $\in$ because RKC-schemes with small $\in$ have an irregular stability region. Figure S5 illustrates the operator spectrum and stability regions of the chosen best RKC scheme of a bristled wing at Re=24. The selected RKC scheme has a significantly larger stability region along the real axis than the RK4 scheme that is shown for comparison. Taking into account the fact that the RKC scheme performs 7 function evaluations per time step while the RK4 uses only 4, the overall speed-up for the RKC amounts to a factor of approximately 10.

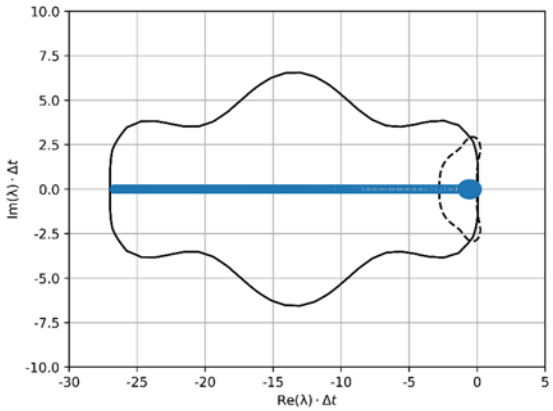

Figure S5. Stability region of best Runge-Kutta-Chebychev scheme (solid line, s=7, $\in$ =1.76) compared to a classical Runge-Kutta 4 scheme (dashed line). Blue dots are eigenvalues of a 1-D, discrete, 2nd order ACM operator with C_0=20, ν=6.95 10^{-2}, K_η=0.5, J_{max}=7, L=4.6, and B_s=23. Data are scaled to a time step corresponding to CFL=0.75. RKC scheme significantly extends the stability region on the real axis. This simulation of a bristled wing at Re=24 requires 1,211,370 function evaluations for a RK4 but only 119,466 for the RKC scheme.

6.3 Validation by a solid rectangular wing

To validate the numerical approach, we used a procedure proposed by Suzuki et al. [12] and refer to previous studies for details [23-24]. The test was done on a single, rectangular flapping wing with finite thickness h = 0.04171R. The wing moved in a horizontal stroke plane at hovering conditions, with positional $\phi = \phi_m \cos(2\pi t)$ and feathering angles $\alpha = \alpha_m (\tanh c_\alpha)^{-1} \tanh(c_\alpha \sin(2\pi t))$. Angles were $\phi_m = 80°$, $\alpha_m = 45°$, and $c_\alpha = 3.3$ (Fig. S6*a*). Free stream velocity was zero and Reynolds number based on mean wing chord (c_m=0.4167R) 100 (see section 4). The size of the computational domain was 6R × 6R × 6R that is slightly larger than in previous publications [19-20]. At the outer border of the domain, we imposed homogeneous Dirichlet conditions, $\underline{u}_\infty = 0$ and $p_\infty = 0$, using sponge technique (see section 6.1). We performed a series of three simulations corresponding to coarse, medium and fine resolutions, with artificial speed of sound, penalization and sponge constants coupled to Δx to ensure convergence (Fig. S6*b*). The selected RKC scheme was s=4 and $\in$ =20, and block size B_s=23. Figure S6*c* shows lift and drag coefficients obtained from this computations including results from the literature. The simulations at medium and fine resolution well agree with results from the literature but at coarse resolution the errors for lift are slightly larger than for drag.

(a)

(b)

	J_{max}	$h/\Delta x$	C_0	C_η	C_ε	C_{sp}
coarse	5	5.1	15	$4.5 \cdot 10^{-4}$	$4 \cdot 10^{-2}$	$1.7 \cdot 10^{-3}$
medium	6	10.2	21	$1.1 \cdot 10^{-4}$	10^{-2}	$1.2 \cdot 10^{-3}$
fine	7	20.5	30	$2.8 \cdot 10^{-4}$	$2.5 \cdot 10^{-3}$	$8.3 \cdot 10^{-4}$

(c)

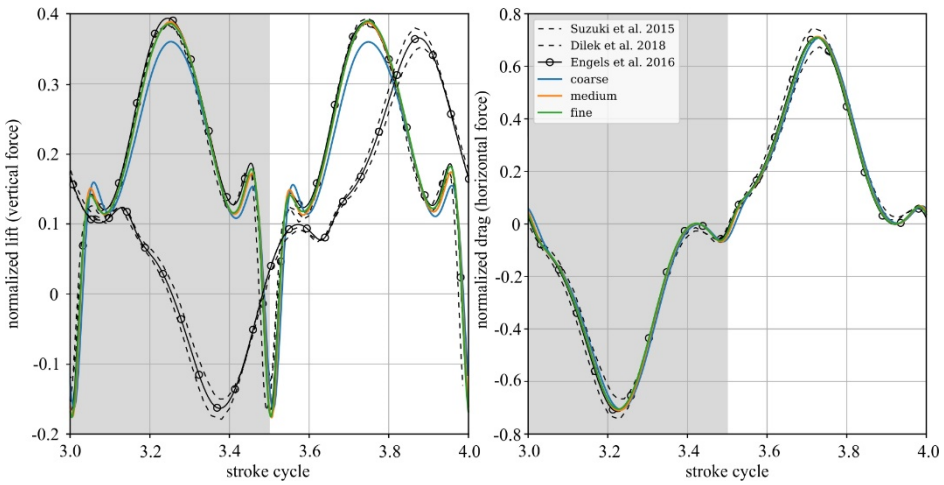

Figure S6. Validation of numerical method. (*a*) Wingbeat kinematics at hovering flight conditions. (*b*) Numerical parameters used in simulations with fine, medium, and coarse resolution. (*c*) Time evolution of normalized lift (vertical force) and normalized drag (horizontal force) and comparison with results from the literature (see text for details).

6.4 Validation and grid convergence for simulations of bristled wings

Our bristled wing modelling approach has been validated in a previous study [6]. We compared simulated forces of a revolving bristled wing with experimental data. That study yielded a set of numerical parameters that ensured good agreement between the simulation and the experiment, in terms of the lift and the drag.

For further validation, we performed convergence tests of our numerical model using bristled wing with Δb=0.054R at Re=14 and flapping with lift-based kinematics (Fig. S7). The single wing was placed in the centre of a cubic domain with size L=4.6 because previous simulations showed that the influence of walls is negligible for this domain size. Wing thickness was 7.7×10^{-3} wing length. Coarse resolution in bristled wings thus compares to fine resolution in the previous test on the membranous wing (cf. section 6.3). Figure S7*a* shows the numerical parameters and figure S7*b* the three components of aerodynamic forces acting on the bristled wing. Data convergence suggests that a resolution $h / \Delta x \approx 5$ is appropriate for the tested Reynolds number. As flow scales increase with decreasing Reynolds number, the above resolution is also appropriate for smaller Reynolds numbers.

(a)

	J_{max}	$h/\Delta x$	C_0	C_η	C_ε	C_{sp}
coarse	7	4.9	20	$9.7 \cdot 10^{-6}$	10^{-2}	$1.2 \cdot 10^{-3}$
medium	8	9.8	28	$2.2 \cdot 10^{-6}$	10^{-2}	$8.2 \cdot 10^{-4}$
fine	9	19.7	40	$5.5 \cdot 10^{-7}$	10^{-2}	$5.8 \cdot 10^{-4}$

(b)

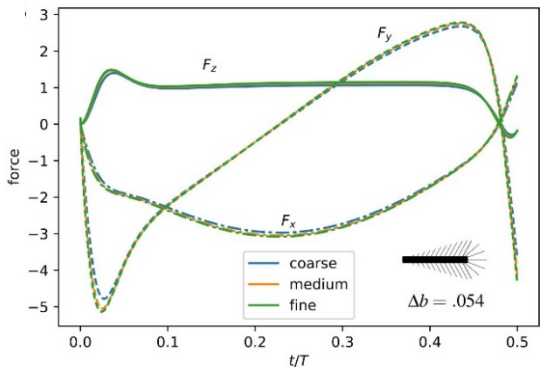

Figure S7. Grid convergence test for a bristled wing with Δb=0.054 at Reynolds number Re=14. (*a*) Numerical parameters used in the simulations. (*b*) Time evolution of the x, y and z components of aerodynamic forces for coarse, medium and fine resolutions. *t*, time; *T*, stroke cycle.

An additional validation, in which we compare simulated forces of a revolving bristled wing with experimental data can be found in a previously published study [6].

6.5 Influence of the domain size

Prior to performing our simulations, we did preliminary tests on the significance of domain size on our numerical results. We tested the solid wing at $Re = 4$ because this case yields (smallest Re) is most sensitive to changes in the domain size. We performed simulations with cubic domain sizes of $L = 4.6$, 9.2 and 18.4 in which we kept resolution constant. Figure S8 illustrates that the resulting lift force is virtually identical in all three cases and that thus the domain with $L = 4.6$ is sufficient for our simulations.

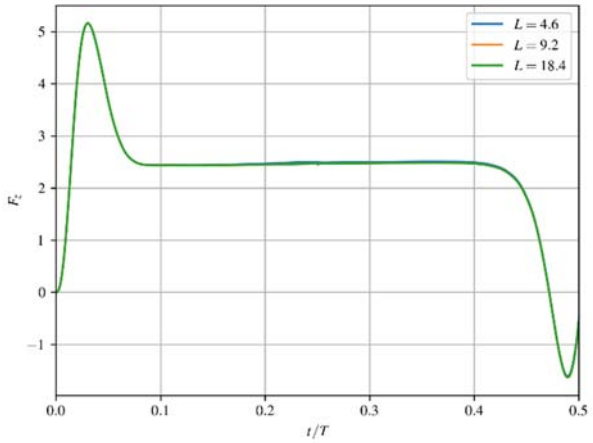

Figure S8. Significance of domain size L on force. Lift is generated by a solid wing in domains with three different sizes (cf. inset). t, time; T, stroke cycle.

Section 7: Rankine-Froude efficiency

Rankine-Froude efficiency is the ratio between the theoretically smallest and the actual aerodynamic power for lift production assuming an idealized, homogeneous and turbulence-free jet downward wake in the vertical direction. We computed this parameter according to Ellington [25] as:

$$\eta = F_z^* \sqrt{\frac{F_z^*}{2\rho A_0}} \left(P_{aero}^*\right)^{-1}, \qquad \text{(eq. S19)}$$

with ρ the density of air and the appropriate total actuator disc area for two wings, i.e.:

$$A_0 = \frac{\Phi R^2}{2}. \qquad \text{(eq. S20)}$$

References

[1] Huber, J.T. & Noyes, J.S. 2013 A new genus and specied of fairyfly, *Tinkerbella nana* (Hymenoptera, Mymaridae), with comments on its sister genus *Kikiki*, and discussion on small size limits in arthropods. *J. Hymenopt. Res.* **32**, 17-44.

[2] Weis-Fogh, T. 1973 Quick estimates of flight fitness in hovering animals, including novel mechanisms for lift production. *J. Exp. Biol.* **59**, 169-230.

[3] Polilov, A.A. 2017 First record of Megaphragma (Hymenoptera, Trichogrammatidae) in Columbia, and third animal species known to have anucleate neurons. *J. Hymenopt. Res.* **60**, 181-185.

[4] Barro, P.J.D., Driver, F., Naumann, I.D., Schmidt, S., Clarke, G.M. & Curran, J. 2000 Descriptions of three species of *Eretmocerus* Haldeman (Hymenoptera: Aphelinidae) parasitising *Bemisia tabaci* (Gennadius)(Hemiptera: Aleyrodidae) and *Trialeurodes vaporariorum* (Westwood)(Hemiptera: Aleyrodidae) in Australia based on morphological and molecular data. *Aust. J. Entomol.* **39**, 259-269.

[5] Cheng, X. & Sun, M. 2018 Very small insects use novel wing flapping and drag principle to generate the weight-supporting vertical force. *J. Fluid Mech.* **855**, 646-670.

[6] Kolomenskiy, D., Farisenkov, S., Engels, T., Lapina, N., Petrov, P., Lehmann, F.-O., Onishi, R., Liu, H. & Polilov, A.A. 2020 Aerodynamic performance of a bristled wing of a very small insect. *Exp. Fluids* **61**, 1-13.

[7] Vincent, J.F.V. & Wegst, U.G.K. 2004 Design and mechanical properties of insect cuticle. *Arthropod. Struct. Dev.* **33**, 187-199. (doi:10.1016/j.asd.2004.05.006).

[8] Dennis, S.C.R. & Shimshoni, M. 1965 The steady flow of a viscous fluid past a circular cylinder. *Aeronautical Research Council* **CP No. 797**.

[9] Cheer, A.Y.L. & Koehl, M.A.R. 1987 Paddles and rakes: fluid flow through bristled appendages of small organisms. *J. Theor. Biol.* **129**, 17-39.

[10] Toomey, J. & Eldredge, J.D. 2008 Numerical and experimental study of the fluid dynamics of a flapping wing with low order flexibility. *Phys. Fluids* **20**, 073603.

[11] Yavorskaya, M.I., Beutel, R.G., Farisenkov, S.E. & Polilov, A.A. 2019 The locomotor apparatus of one of the smallest beetles – the thoracic skeletomuscular system of *Nephanes titan* (Coleoptera, Ptiliidae). *Arthropod Struct. Dev.* **48**, 71-82.

[12] Suzuki, K., Minami, K. & Inamuro, T. 2015 Lift and thrust generation by a butterfly-like flapping wing-body model: immersed boundary-lattice Boltzmann simulations. *J. Fluid Mech.* **767**, 659-695.

[13] Engels, T., Kolomenskiy, D., Schneider, K., Lehmann, F.-O. & Sesterhenn, J. 2016 Bumblebee flight in heavy turbulence. *Phys. Rev. Lett.* **116**, 028103. (doi:10.1103/PhysRevLett.116.028103).

[14] Lehmann, F.-O. & Dickinson, M.H. 1998 The control of wing kinematics and flight forces in fruit flies (*Drosophila* spp.). *J. Exp. Biol.* **201**, 385-401.

[15] Ohwada, T. & Asinari, P. 2010 Artificial compressibility method revisited: Asymptotic numerical method for incompressible Navier–Stokes equations. *J. Comp. Phys.* **229**, 1698–1723.

[16] Chorin, A.J. 1967 A numerical method for solving incompressible viscous flow problems. *J. Comp. Phys.* **2**, 12-26.

[17] Angot, P., Bruneau, C. & Fabrie, P. 1999 A penalization method to take into account obstacles in incompressible viscous flows. *Numer. Math.* **81**, 497–520.

[18] Jones, S.K., Yun, Y.J.J., Hedrick, T.L., Griffith, B.E. & Miller, L.A. 2016 Bristles reduce the force required to 'fling' wings apart in the smallest insects. *J. Exp. Biol.* **219**, 3759–3772.

[19] Engels, T., Schneider, K., Reiss, J. & Farge, M. 2021 A wavelet-adaptive method for multiscale simulation of turbulent flows in flying insects. *Commun. Comput. Phys.*, arXiv:1912.05371.

[20] Engels, T., Wehmann, H.-N. & Lehmann, F.-O. 2020 Three-dimensional wing structure attenuates aerodynamic efficiency in flapping fly wings. *J. R. Soc. Interface* **17**, 20190804. (doi:10.1098/rsif.2019.0804).

[21] Verwer, J.G., Hundsdorfer, W.H. & Sommeijer, B.P. 1989 Convergence Properties of the Runge-Kutta-Chebyshev Method. *Numer. Math.* **57**, 157-178.

[22] Verwer, J.G., Sommeijer, B.P. & Hundsdorfer, W.H. 2004 RKC time-stepping for advection–diffusion–reaction problems. *J. Comp. Phys.* **201**, 61-79.

[23] Engels, T., Kolomenskiy, D., Schneider, K. & Sesterhenn, J. 2015 FluSI: A novel parallel simulation tool for flapping insect flight using a Fourier method with volume penalization. *SIAM J. Sci. Comp.* **38**, S3-S24.

[24] Dilek, E., Erzincanli, B. & Sahin, M. 2019 The numerical investigation of Lagrangian and Eulerian coherent structures for the near wake structure of a hovering *Drosophila*. *Theor. Comp. Fluid Dyn.* **33**, 255-279.

[25] Ellington, C.P. 1984 The aerodynamics of hovering insect flight. V. A vortex theory. *Phil. Trans. R. Soc. Lond. B* **305**, 115-144.